nature materials

ARTICLES

https://doi.org/10.1038/s41563-019-0379-3

Formation of aligned periodic patterns during the crystallization of organic semiconductor thin films

John S. Bangsund[1], Thomas R. Fielitz[1,2], Trevor J. Steiner[1], Kaicheng Shi[1], Jack R. Van Sambeek[1], Catherine P. Clark[1] and Russell J. Holmes[1*]

Self-organizing patterns with micrometre-scale features are promising for the large-area fabrication of photonic devices and scattering layers in optoelectronics. Pattern formation would ideally occur in the active semiconductor to avoid the need for further processing steps. Here, we report an approach to form periodic patterns in single layers of organic semiconductors by a simple annealing process. When heated, a crystallization front propagates across the film, producing a sinusoidal surface structure with wavelengths comparable to that of near-infrared light. These surface features initially form in the amorphous region within a micrometre of the crystal growth front, probably due to competition between crystal growth and surface mass transport. The pattern wavelength can be tuned from 800 nm to 2,400 nm by varying the film thickness and annealing temperature, and millimetre-scale domain sizes are obtained. This phenomenon could be exploited for the self-assembly of microstructured organic optoelectronic devices.

Methods for spontaneously forming periodic surface structures at the nanometre or micrometre scale have received considerable attention for lithography-free patterning applications[1–6]. Spontaneous pattern formation is attractive as it can be easily scaled to large areas, potentially enabling higher throughput and lower cost than serial processes[1,7]. These self-assembly techniques have primarily exploited phase separation of block copolymers or strain-induced wrinkling of polymeric thin films. Block copolymers are effective for patterning sub-100-nm features[7–9], but are not amenable to creating features on the length scale of visible light. Thin-film wrinkling can form structures with periodicities ranging from ~400 nm–10 μm (ref. [10]), and is hence suitable for optoelectronic and photonic applications in the visible and near-infrared region[11–15]. Although wrinkling approaches have afforded remarkable control and tunability over pattern formation, aligned patterns are more challenging to realize, and often require the application of anisotropic stress during film deposition or additional patterning[2,10,16]. Furthermore, these approaches rely on the use of multiple layers and often lack thermal stability[17,18].

Here, we report a crystallization-mediated mechanism in which aligned, periodic surface structures are formed along the amorphous-to-crystal transformation front during annealing of single-layer thin films of small-molecule organic semiconductors. The observed topography originates in the form of material depletion and accumulation in the amorphous region within ~0.5 μm of the crystal front, probably due to mass-transport-limited crystal growth. These patterns seem to be related to structures that form during banded-spherulitic growth of various polymers and small molecules[19–21], growth of hexagonal lamellar crystals of isotactic polystyrene[22], polymorph transformations in the small molecule 5-methyl-2-[(2-nitrophenyl)amino]-3-thiophenecarbonitrile (ROY)[23] and explosive crystallization of amorphous Si[24].

The current work is distinguished from these previous demonstrations by several promising features, including: large-area pattern coverage with millimetre-scale single-crystal domains, direct integration into single layers of organic semiconductors, feature depths that span nearly the entire film thickness and pattern wavelengths that are tunable over a range useful for optoelectronic applications. The periodicity of the observed wrinkling can be tuned from 800 nm to 2,400 nm by varying the film thickness and annealing temperature. The resulting structures exhibit excellent thermal stability as they occur with a transition to a crystalline phase.

As many organic semiconducting molecules form glasses when deposited and crystallize readily when annealed[25], the crystallization-mediated periodic patterning method reported here may be generalizable to a wide range of materials. Indeed, we report pattern formation in four archetypical organic semiconductors. This phenomenon could find applications in a variety of optoelectronic settings, including the improvement of light trapping in solar cells[14], enhancing light extraction from emissive devices[15,26,27] and the fabrication of self-assembled organic lasers[12,28].

Formation and tunability of aligned periodic patterns

Pattern formation was examined by annealing organic semiconductor thin films on Si substrates at temperatures of 20–80 °C above their bulk glass transition temperature (T_g). Although several materials are observed to form periodic surface structure, we first provide a comprehensive analysis using 2,2′,2″-(1,3,5-benzinetriyl)-tris(1-phenyl-1-H-benzimidazole) (TPBi, Fig. 1a), a common electron-transporting material in organic light-emitting devices (OLEDs). As-deposited films of TPBi appear smooth and featureless, typical of glassy vapour-deposited films. When annealed above $T_g \approx 124$ °C (ref. [25]) in the range of 150–185 °C, TPBi films crystallize readily and spontaneously form periodic undulations perpendicular to the direction of growth (Fig. 1).

The pattern periodicity, d, increases monotonically with annealing temperature, ranging from 1.20 ± 0.05 μm at 155 °C to 1.48 ± 0.05 μm at 175 °C for a 30-nm-thick film (Fig. 1e–h and Fig. 2c). In the range of 160–175 °C, the crystal growth front is smooth and continuous, resulting in a highly aligned grating topography with millimetre-sized grains (Fig. 1c,d). At higher temperatures (180 °C, Fig. 1h), the film transformation occurs more

[1]Department of Chemical Engineering and Materials Science, University of Minnesota, Minneapolis, MN, USA. [2]Present address: The Dow Chemical Company, Midland, MI, USA. *e-mail: rholmes@umn.edu

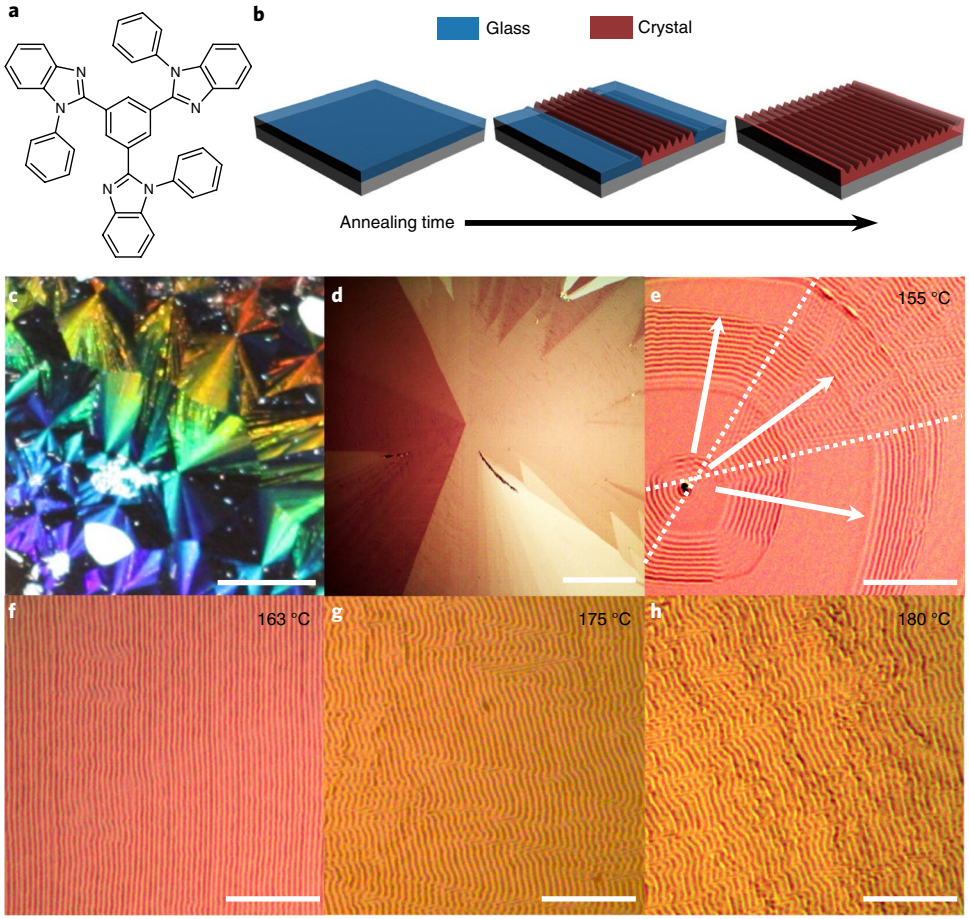

Fig. 1 | Periodic pattern formation in TPBi films and dependence on temperature. a, Molecular structure of TPBi. **b**, Schematic depicting amorphous (blue) to crystalline (red) transformation that propagates across the TPBi film when it is annealed for several minutes at a temperature above 150 °C, leading to large-area pattern formation. **c**, Macroscopic photo of optical diffraction from a 30-nm-thick TPBi film on Si annealed at 170 °C. The sample is illuminated by unpolarized white light at an oblique angle. Note that dark regions are due to the orientation of the corrugation relative to the illumination source and are diffractive at different viewing angles. Scale bars for **a**–**c**, 0.5 cm. **d**, Cross-polarized optical micrograph of 30-nm-thick TPBi annealed at 170 °C showing a millimetre-scale crystalline grain. Scale bar, 0.5 mm. **e**–**h**, Unpolarized optical micrographs of 30-nm-thick TPBi films on Si substrates annealed at various temperatures. **e**, 155 °C with periodicity $d = 1.20 \pm 0.05$ μm. Arrows indicate the growth direction of three crystal facets from a single nucleation point. The slower-growing facets (top and bottom regions) show plateau regions without periodic topography. **f**, 163 °C with $d = 1.25 \pm 0.06$ μm, showing exquisite alignment of the periodic ridges. **g**, 175 °C with $d = 1.48 \pm 0.05$ μm. **h**, 180 °C with $d = 1.51 \pm 0.12$ μm. These images show a more disordered topography due to the higher growth rate at high temperatures. Scale bars for **e**–**h**, 20 μm.

rapidly along an uneven growth front, producing more disordered structures. Below 160 °C, corrugation along certain growth directions is occasionally interrupted by plateaus (155 °C, Fig. 1e). Films annealed below 150 °C instead show faceted growth rings with irregular spacings (Supplementary Fig. 1), similar to structures previously observed in rubrene[29]. This transition from periodic topography to growth rings at lower temperatures suggests that both surface features arise from the same physical mechanism.

Two crystalline phases of TPBi can form over the temperature range of interest. The phase that shows periodic corrugation forms relatively smooth, platelet-like grains (Fig. 1d) and covers >90% of the film surface at annealing temperatures below 170 °C and above ~180 °C. A second phase that has a dendritic morphology and increased roughness becomes more dominant between 170 °C and 180 °C, with surface coverage ranging from 20–80% (Supplementary Fig. 2). Diffraction of visible light can also be observed in these images, illustrating that the periodic surface structures have nearly complete surface coverage in the platelet-like grains. It is worth noting that these crystals are not spherulites, in contrast to banded spherulites[30]. As shown in Fig. 1d and below in Fig. 3a, extinction in cross-polarized optical micrographs is uniform within a crystalline grain, indicating that these platelet-like grains consist of a single crystal orientation[19,29,31].

The pattern periodicity observed in TPBi shows a roughly linear dependence on film thickness, ranging from $d = 0.83 \pm 0.09$ μm for an 18-nm-thick film to $d = 2.38 \pm 0.14$ μm for a 47-nm-thick film at a constant temperature of 165 °C (Fig. 2c). The periodicity is determined from fast Fourier transforms (FFTs) of optical micrographs and checked for consistency with measurements from atomic force microscopy (AFM) images (Fig. 2d–g) and diffraction (Fig. 2a,b and Supplementary Fig. 3). Histograms showing batch-to-batch variability and the distributions used to calculate the confidence intervals in Fig. 2c are included in Supplementary Fig. 4. A statistical analysis of the pattern quality (that is, the degree of alignment and order) is also discussed in the Supplementary Information, and the variability in pattern quality is shown and quantified across multiple samples in Supplementary Figs. 5–8.

Under ex situ AFM (Fig. 2d–g), the films show well-defined periodicity that is nearly sinusoidal, with wavelengths of 0.77 ± 0.10 μm, 1.2 ± 0.1 μm and 1.8 ± 0.1 μm for 18-, 28- and 42-nm-thick films

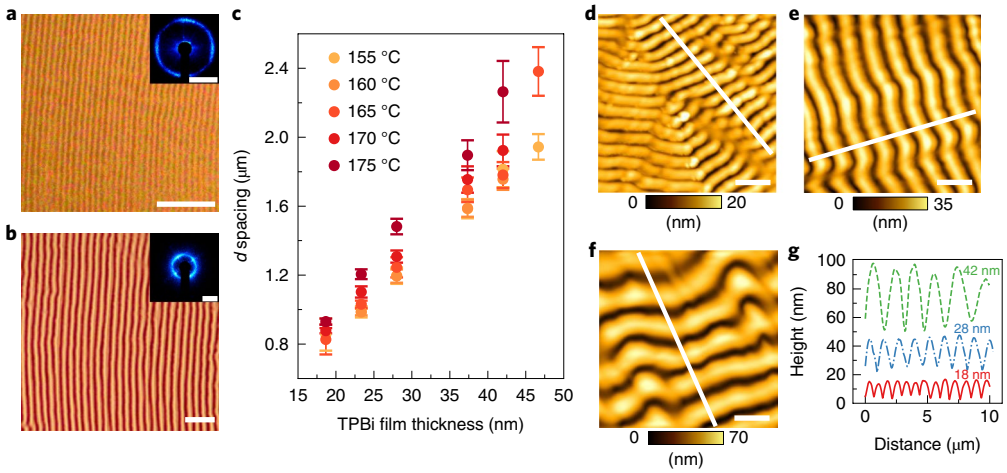

Fig. 2 | Characterization of pattern tunability and surface topography. a, A 25-nm-thick film of TPBi on Si annealed at 165 °C with $d = 1.03 \pm 0.03$ μm. Scale bar, 10 μm. Inset, a diffraction pattern produced by illuminating the sample with a laser of wavelength $\lambda = 473$ nm (scale bar, 1 μm^{-1}). **b**, 47-nm-thick TPBi film on Si annealed at 165 °C showing $d = (2.38 \pm 0.14)$ μm. Scale bar, 10 μm. Inset, a diffraction pattern (scale bar, 0.47 μm^{-1}). The inset images in **a** and **b** are both 11.9 cm wide (see Methods). **c**, Dependence of pattern *d* spacing on film thickness and temperature, as extracted from fast Fourier transforms of optical microscopy images. Error bars are the 95% confidence intervals determined using the Student's *t*-distribution for small sample sizes and averaged over at least ten images. **d**–**f**, AFM height images of TPBi films on Si annealed at 165 °C with thicknesses of 18 nm (**d**), 28 nm (**e**) and 42 nm (**f**). Scale bars, 2 μm in **d**–**f**. **g**, Height profiles for 18-, 28- and 42-nm-thick TPBi films. The profiles are vertically offset for clarity. The pattern periodicities extracted from these profiles (0.77 μm, 1.2 μm and 1.8 μm, respectively) are consistent with measurements from optical microscopy. The average peak-to-valley amplitudes extracted from these profiles are 13 nm, 22 nm and 42 nm, respectively.

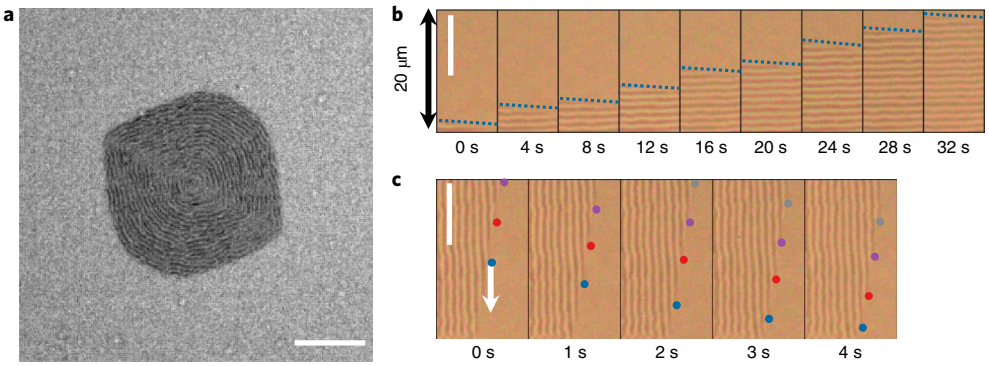

Fig. 3 | In situ optical microscopy of periodic pattern formation during annealing. a, Cross-polarized optical micrograph of a single crystalline grain in a 30-nm-thick TPBi film during annealing at 165 °C. The grating pattern is aligned parallel to the growth front and is only observed within the crystallized region. The surrounding material with lower extinction is amorphous, showing no birefringence, unlike the crystalline grain. Scale bar, 20 μm. **b**, Time series of unpolarized optical micrographs during annealing of a 30-nm-thick TPBi film at 165 °C, showing pattern formation along the boundary of the amorphous-to-crystalline transformation front that propagates at a rate of ~0.6 μm s^{-1}. The time between frames is 4 s; scale bar, 10 μm. Dashed lines indicate the edge of the crystalline growth front. **c**, Finer time steps (1 s between frames) of the same region in **b**, showing individual ridges extending along the length of the growth front at a rate of ~3 μm s^{-1}. The coloured circles mark the endpoints of each individual ridge. Scale bar, 10 μm. The source video for **b** and **c** is provided in the Supplementary Information.

of TPBi annealed at 165 °C, in good agreement with the values extracted from optical micrographs. The peak-to-valley amplitude increases with film thickness from 13 ± 1 nm for an 18-nm-thick film to 22 ± 2 nm for a 28-nm-thick film and 42 ± 7 nm for a 42-nm-thick film. The peak-to-valley amplitude is almost as large as the full thickness for a 42-nm-thick film, and over 70% of the film thickness for 18- and 28-nm-thick films.

Pattern formation mechanism

Films were imaged in situ during annealing to study the formation of the structures. The time evolution of the growth front for a 30-nm-thick film annealed at 165 °C is shown in Fig. 3. The periodic pattern is formed as the crystal growth front progresses (at ~0.6 μm s^{-1}), with the ridges appearing at the left side of the image window of Fig. 3b and then extending along the length of the growth front. Cross-polarized micrographs on the same film show birefringence contrast progressing simultaneously with the onset of the periodic features, indicating that height variations form concurrently with crystallization (Fig. 3a). Finer time steps showing individual ridges progressing laterally across the growth front at a rate of ~3 μm s^{-1} are presented in Fig. 3c. These time series are taken along the slower-growing crystal facet, suggesting that growth of the crystal along this direction occurs partly via molecular attachment on the faster-growing crystal plane[29]. The crystallinity of the transformed material was confirmed with X-ray diffraction (Supplementary Fig. 9). Once formed, these patterns show a fixed spacing and are thermally

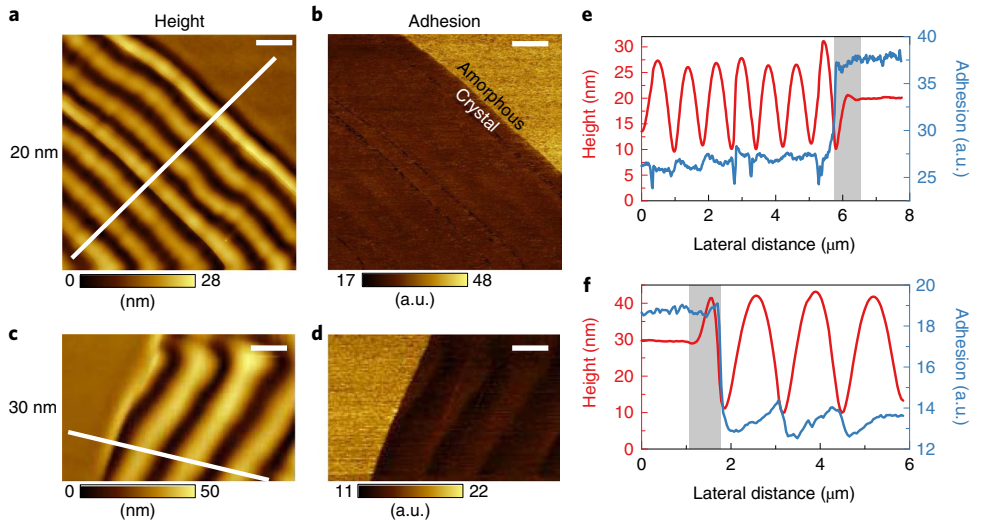

Fig. 4 | Topography and mechanics near the crystal growth front. a,**b**, Height (**a**) and adhesion (**b**) images for 20-nm-thick TPBi on Si annealed at 163 °C. Scale bars are 1 μm. **c**,**d**, Height (**c**) and adhesion (**d**) images for 30-nm-thick TPBi on Si annealed at 165 °C. Scale bars, 1 μm. All images are acquired with PF-QNM AFM. **e**,**f**, Height and adhesion profiles across the crystal growth front are shown for 20-nm-thick (**e**) and 30-nm-thick (**f**) TPBi, respectively. The white lines in **a** and **c** correspond to the centre lines for the height and adhesion profiles plotted in **e** and **f**, with profiles averaged laterally over 10 pixels in the perpendicular direction. The adhesion images provide contrast between crystalline and untransformed amorphous regions, due the differences in the mechanical properties of the two phases. The shaded regions in **e** and **f** highlight the portion of the amorphous region near the crystal growth front that shows both accumulation and depletion of material.

stable, with no significant change in periodicity or morphology after post-annealing for several hours at 150 °C (Supplementary Fig. 10). Thermal stability seems to be limited by sublimation loss[29].

The crystal growth rate increases exponentially with temperature and modestly with film thickness, with 40-nm-thick films showing ~30% faster growth rates than 20-nm-thick films. The film thickness trend probably arises due to the film–substrate interaction[32,33]. In correlation with growth rate, the topography becomes more disordered with increases in either temperature (Fig. 1) or film thickness (Supplementary Fig. 11). Higher disorder is also observed along the faster-growing facets of TPBi crystals (Supplementary Fig. 12), suggesting that the pattern quality depends on the transformation front velocity. The growth rate evidently also plays a role in the formation of the smooth regions seen at temperatures below 160 °C (Fig. 1e), as only the slower-growing facets form these plateaus. Absolute growth rates are probably less important than the velocity relative to other kinetic factors, such as the mobility of the supercooled liquid, as fast-growing facets show higher disorder across a range of annealing temperatures with growth rates of ~0.5–3 μm s^{-1}.

To probe how the surface topography forms at the growth front, partially crystallized films were examined ex situ with peak force quantitative nanomechanical (PF-QNM) AFM, which allows amorphous and crystalline regions to be distinguished by their mechanical properties. A stark contrast in adhesion is seen between these regions (Fig. 4b,d), where the amorphous material exhibits greater adhesion, reflecting the increased degrees of freedom for molecular rearrangement and interaction with the tip. Strikingly, the onset of surface height variations does not coincide with the grain boundary, but extends ~0.5 μm into the surrounding amorphous material (Fig. 4e,f) with both significant accumulation and depletion in this region. This indicates that the periodic topography originates here, rather than solely in the crystal.

This behaviour seems distinct from conventional diffusion-limited crystal growth, which is characterized by a depletion zone surrounding the growth front[32,34,35], where only the crystal rises above the height of the as-deposited film due to upward growth by surface diffusion[36]. However, these height profiles resemble the damped-oscillation solutions yielded by the Mullins model for surface diffusion and a similar model for viscous surface flow at steady state[34,37,38], and share features with the depletion and halo regions recently reported during the crystallization of isotactic polystyrene[22]. These similarities suggest that this periodic surface topography arises due to a competition between long-range mass transport and crystal growth[39]. The observed height variations could then be explained by a cyclical process. Initially, crystal growth outpaces long-range mass transport leading to depletion of material in the region near the growth front. Growth then slows at high depletion, due to the reduced availability of material and increased substrate interactions[22,33], allowing mass transport to replenish the depleted region and increase the height of the accumulation region. As the region leading the crystal front thickens, growth will again accelerate and restart the cycle. Mass transport here is probably dominated by viscous flow and not surface diffusion, as annealing is performed 20–60 °C above T_g, well above the reported transition between these regimes for common molecular glasses[40]. The role of surface transport in pattern formation is confirmed by experiments that employed capping layers to suppress surface molecular motion. Only smooth crystals without periodic topography formed in TPBi capped with 10-nm-thick films of Au or a high-T_g organic material (Supplementary Fig. 13).

Substrate interactions become important for these confined films[41], and hence bulk crystallization and surface crystallization may both be active[34,42]. Surface crystallization is probably responsible for the formation of depletion and accumulation features, whereas bulk crystallization may continue to drive growth when the depletion depth becomes large and limits the supply of material for surface growth. In capped TPBi films, the crystal growth rate is reduced by 50–90% compared with uncapped films but is not entirely deactivated. This confirms that transport at the free surface is the primary mechanism that feeds crystal growth, but that crystallization in the bulk of the film constitutes a non-negligible contribution. Several other effects may contribute to the observed patterns. The volume change on crystallization may induce stresses in the surrounding amorphous material, providing a driving force for the formation of surface features. Mobility near the growth front

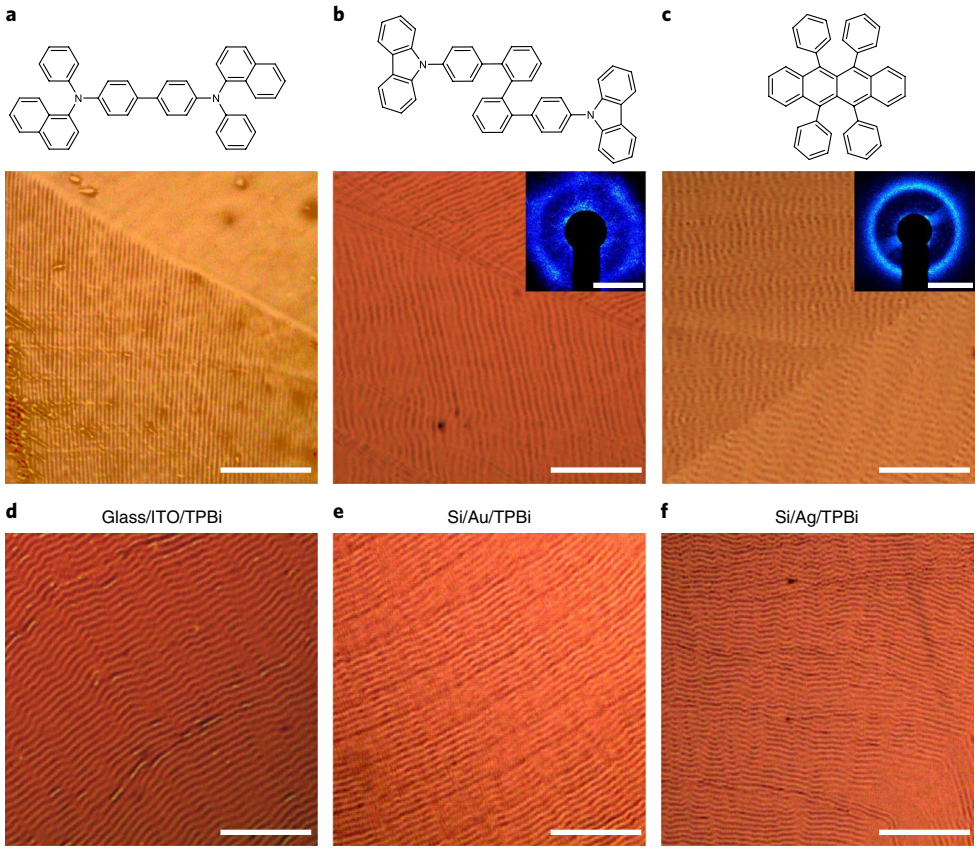

Fig. 5 | Pattern formation in other organic semiconductors and on common electrode surfaces. a–c, Molecular structures (top) and unpolarized optical microscope images of pattern formation (bottom) in a 30-nm-thick film of α-NPD annealed at 170 °C with $d = 0.98 \pm 0.05$ μm (**a**), a 35-nm-thick film of BCBP annealed at 170 °C with $d = 1.6 \pm 0.1$ μm (**b**) and a 30-nm-thick film of rubrene annealed at 185 °C with $d = 1.75 \pm 0.1$ μm (**c**). The insets in **b** and **c** are diffraction images of the same films with scale bars of 0.64 μm^{-1} and 0.57 μm^{-1}, respectively, and the same physical width (6.8 cm). Diffraction was not observable for α-NPD due to the incomplete surface coverage of the pattern, with the majority of the film forming flat crystalline regions as shown in the upper right corner of the image in **a**. Samples in **a–c** were prepared on Si substrates. **d–f**, Unpolarized optical microscope images of pattern formation in 30-nm-thick TPBi film deposited on common electrode surfaces: Glass/ITO (**d**), Si/Au (**e**) and Si/Ag (**f**). All films were annealed at 163 °C. Scale bars, 20 μm for all optical microscope images.

may also be periodically enhanced by the release of heat from fusion or from tension arising from crystallization[24,43].

Assuming this mechanism of pattern formation, the increase in pattern wavelength at higher annealing temperatures may stem from the mobility of the supercooled liquid having a steeper function of temperature than the crystal growth rate, allowing flow to occur over a larger distance. This interpretation should lead to some flattening of the pattern features, in qualitative agreement with AFM measurements that show a decreased amplitude at annealing temperatures >175 °C (Supplementary Fig. 14). The dependence of the pattern wavelength on thickness could partially be a consequence of the variation in T_g and growth rate with film thickness[41,44], and also the total supply of material (that is, thicker films take longer to deplete, allowing more time for the width of the depletion zone to increase)[22]. The flat regions at low temperatures (Fig. 1e and Supplementary Fig. 1) probably form due to mass transport rates matching or exceeding crystal growth, preventing the formation of depletion regions.

Alternative molecules and surfaces for pattern formation

To enable device integration, it is important to realize patterns in other organic semiconductors and on common electrode surfaces. As many vapour-deposited organic semiconductors form glassy films and crystallize above T_g, a variety of materials may be amenable to crystallization-mediated patterning. We have observed periodic pattern formation in the hole-transport material N,N′-bis(naphthalen-1-yl)-N,N′-bis(phenyl)-benzidine (α-NPD), the ambipolar host material 2,2'-bis(4-(carbazol-9-yl)phenyl)-biphenyl (BCBP) and the archetypical organic semiconductor rubrene. α-NPD (bulk $T_g = 95$ °C)[45] forms a pattern with $d = 0.98 \pm 0.05$ μm for a 30-nm-thick film annealed at 170 °C (Fig. 5a). BCBP (bulk $T_g = 120$ °C)[46] forms a pattern with $d = 1.6 \pm 0.1$ μm for a 35-nm-thick film annealed at 170 °C (Fig. 5b). Rubrene crystallizes above ~115 °C (refs. [29,31]), and forms a pattern with $d = 1.75 \pm 0.1$ μm for a 30-nm-thick film annealed at 185 °C (Fig. 5c). Although the quality and surface coverage of periodic patterns in these materials have not been fully optimized, differences in the molecular structures and T_g suggest that the method is generalizable, and that the pattern periodicity could be further tuned by varying the properties of the materials. The formation of these patterns in both electron- and hole-transporting materials demonstrates the flexibility of this method for device integration.

As a base criterion for pattern formation, a candidate material must form a glassy film that transforms to large-area, platelet-like crystals when annealed. However, due to the observed impact of crystal growth rate on pattern quality, it is likely that a balance of kinetic and thermodynamic factors such as T_g, steric bulk and the supercooled liquid viscosity will determine whether surface structures will form on crystallization. Crystal structure does not seem to impact whether periodic topography forms during crystallization.

The phase of rubrene here has an orthorhombic crystal structure[29], whereas α-NPD is most probably triclinic[47]. The thin-film crystal structures of BCBP and TPBi are yet to be determined.

To inform device integration and assess the potential for direct pattern formation on electrode surfaces, TPBi films were deposited and annealed on a variety of surfaces. We observe pattern formation on common electrode materials such as ITO, Au and Ag (Fig. 5d–f), as well as other substrates, such as Al_2O_3, quartz, glass and WO_3-coated Si (Supplementary Figs. 15 and 16). The substrate was observed to impact crystal growth rate, in agreement with previous work on rubrene in which more hydrophobic substrates decreased the crystal growth rate[32]. The pattern wavelength decreases modestly in substrates with slower crystal growth rates, possibly reflecting substrate interactions that inhibit molecular motion in the supercooled liquid and thus lower the width of the depletion zone. For example, the crystal growth rate in 34-nm-thick TPBi films is reduced from $0.4\,\mu m\,s^{-1}$ on Si/SiO_2 substrates to $0.15\,\mu m\,s^{-1}$ on Si/Au substrates, and the pattern wavelength decreases from $1.46 \pm 0.05\,\mu m$ to $1.32 \pm 0.05\,\mu m$.

Strategies to improve the control of pattern formation

To tailor patterns for arbitrary applications, greater control over long-range pattern alignment, pattern quality and feature depth is needed. As these patterns form along crystal growth fronts, alignment across a sample is limited by grain size. Millimetre-scale domains are achieved here (Fig. 1c,d), and could be further expanded by selecting optimal underlayers[31]. However, long-range alignment is not needed for many applications where randomly-oriented periodic structures can be tolerated or are even desired. For example, outcoupling enhancement layers for OLEDs often consist of random structures to minimize viewing angle dependencies[48].

The pattern quality could be engineered by tuning substrate surface properties to control growth rate[32]. As a demonstration of this strategy, we compared pattern quality and crystal morphology in TPBi films on Si/SiO_2 and Si/Au substrates (Supplementary Figs. 17 and 18). The reduced crystal growth rate on Si/Au substrates leads to smoother growth fronts and improved pattern quality across all tested annealing temperatures. Another route is to use low-T_g underlayer materials[31], which have been shown to increase grain size, reduce branching and reduce nucleation of other phases in rubrene. Additives or mixtures could also be employed to alter the crystal growth rate and shape by suppressing molecular attachment to certain crystal facets[49].

Feature depths of at least 70 nm are typically desired for optoelectronic applications[27,28], and future work should therefore focus on increasing the pattern depth. One strategy to achieve larger amplitudes is to improve the quality of pattern formation in thicker films using the above methods. As the peak-to-valley amplitude can exceed 90% of the film thickness, sufficient depths should be obtained in ~70-nm-thick films.

Outlook

In summary, we report a crystallization-mediated mechanism for the spontaneous formation of highly aligned periodic structures in organic semiconductor thin films. These features develop during annealing along the periphery of the crystal growth front—probably due to competition between crystal growth and surface mass transport—and are quickly incorporated into the crystal grain, producing a sinusoidal surface topography. The wavelength of these structures can be tuned over a broad range from 800 nm to 2,400 nm by changing the film thickness. We show that these patterns are thermally stable and can form on a variety of electrode materials, enabling direct integration into optoelectronic devices. Multiple glassy organic semiconductors are found to form these periodic patterns, suggesting that this method could be generally applied to any readily crystallized materials. We find that crystal growth rate is an important factor in determining whether periodic patterns will form and the overall pattern quality. Owing to its simplicity, this phenomenon could be exploited for low-cost lithography-free patterning and provides a novel assembly method for nanostructured organic optoelectronics.

Online content

Any methods, additional references, Nature Research reporting summaries, source data, statements of code and data availability and associated accession codes are available at https://doi.org/10.1038/s41563-019-0379-3.

Received: 6 July 2018; Accepted: 17 April 2019;
Published online: 03 June 2019

References

1. Schweikart, A., Horn, A., Böker, A. & Fery, A. in *Complex Macromolecular Systems I* 75–99 (Springer, 2009).
2. Chung, J. Y., Nolte, A. J. & Stafford, C. M. Surface wrinkling: a versatile platform for measuring thin-film properties. *Adv. Mater.* **23**, 349–368 (2011).
3. Li, B., Cao, Y.-P., Feng, X.-Q. & Gao, H. Mechanics of morphological instabilities and surface wrinkling in soft materials: a review. *Soft Matter* **8**, 5728–5745 (2012).
4. del Campo, A. & Arzt, E. Fabrication approaches for generating complex micro- and nanopatterns on polymeric surfaces. *Chem. Rev.* **108**, 911–945 (2008).
5. Mei, Y., Kiravittaya, S., Harazim, S. & Schmidt, O. G. Principles and applications of micro and nanoscale wrinkles. *Mater. Sci. Eng. R* **70**, 209–224 (2010).
6. Lacour, S. P., Wagner, S., Huang, Z. & Suo, Z. Stretchable gold conductors on elastomeric substrates. *Appl. Phys. Lett.* **82**, 2404–2406 (2003).
7. Park, M., Harrison, C., Chaikin, P. M., Register, R. A. & Adamson, D. H. Block copolymer lithography: periodic arrays of ~10^{11} holes in 1 square centimeter. *Science* **276**, 1401–1404 (1997).
8. Bates, C. M., Maher, M. J., Janes, D. W., Ellison, C. J. & Willson, C. G. Block copolymer lithography. *Macromolecules* **47**, 2–12 (2014).
9. Segalman, R. A. Patterning with block copolymer thin films. *Mater. Sci. Eng. R* **48**, 191–226 (2005).
10. Bowden, N., Huck, W. T. S., Paul, K. E. & Whitesides, G. M. The controlled formation of ordered, sinusoidal structures by plasma oxidation of an elastomeric polymer. *Appl. Phys. Lett.* **75**, 2557–2559 (1999).
11. Palmer, C. & Loewen, E. *Diffraction Grating Handbook* (Newport Corporation, 2005).
12. Samuel, I. D. W. & Turnbull, G. A. Organic Semiconductor Lasers. *Chem. Rev.* **107**, 1272–1295 (2007).
13. Lu, C., Möhwald, H. & Fery, A. A lithography-free method for directed colloidal crystal assembly based on wrinkling. *Soft Matter* **3**, 1530–1536 (2007).
14. Kim, J. B. et al. Wrinkles and deep folds as photonic structures in photovoltaics. *Nat. Photon.* **6**, 327–332 (2012).
15. Koo, W. H. et al. Light extraction from organic light-emitting diodes enhanced by spontaneously formed buckles. *Nat. Photon.* **4**, 222–226 (2010).
16. Guo, C. F. et al. Path-guided wrinkling of nanoscale metal films. *Adv. Mater.* **24**, 3010–3014 (2012).
17. Kim, J. & Lee, H. H. Wave formation by heating in thin metal film on an elastomer. *J. Polym. Sci. B* **39**, 1122–1128 (2001).
18. Chan, P. E. et al. Viscoelastic properties of confined polymer films measured via thermal wrinkling. *Soft Matter* **5**, 4638–4641 (2009).
19. Shtukenberg, A. G., Punin, Y. O., Gunn, E. & Kahr, B. Spherulites. *Chem. Rev.* **112**, 1805–1838 (2012).
20. Woo, E. M. & Lugito, G. Origins of periodic bands in polymer spherulites. *Eur. Polym. J.* **71**, 27–60 (2015).
21. Crist, B. & Schultz, J. M. Polymer spherulites: a critical review. *Prog. Polym. Sci.* **56**, 1–63 (2016).
22. Poudel, P., Majumder, S., Chandran, S., Zhang, H. & Reiter, G. Formation of periodically modulated polymer crystals. *Macromolecules* **51**, 6119–6126 (2018).
23. Sun, Y., Xi, H., Chen, S., Ediger, M. D. & Yu, L. Crystallization near glass transition: transition from diffusion-controlled to diffusionless crystal growth studied with seven polymorphs. *J. Phys. Chem. B* **112**, 5594–5601 (2008).
24. Ohdaira, K., Fujiwara, T., Endo, Y., Nishizaki, S. & Matsumura, H. Explosive crystallization of amorphous silicon films by flash lamp annealing. *J. Appl. Phys.* **106**, 044907 (2009).
25. Tao, Y., Yang, C. & Qin, J. Organic host materials for phosphorescent organic light-emitting diodes. *Chem. Soc. Rev.* **40**, 2943–2970 (2011).
26. Meerholz, B. K. & Müller, D. C. Outsmarting waveguide losses in thin-film light-emitting diodes. *Adv. Funct. Mater.* **11**, 251–253 (2001).

27. Fuchs, C. et al. Quantitative allocation of Bragg scattering effects in highly efficient OLEDs fabricated on periodically corrugated substrates. *Opt. Express* **21**, 16319–16330 (2013).
28. Kuehne, A. J. C. & Gather, M. C. Organic lasers: recent developments on materials, device geometries, and fabrication techniques. *Chem. Rev.* **116**, 12823–12864 (2016).
29. Fielitz, T. R. & Holmes, R. J. Crystal morphology and growth in annealed rubrene thin films. *Cryst. Growth Des.* **16**, 4720–4726 (2016).
30. Xu, J. et al. Direct AFM observation of crystal twisting and organization in banded spherulites of chiral poly(3-hydroxybutyrate-co-3-hydroxyhexanoate). *Macromolecules* **37**, 4118–4123 (2004).
31. Fusella, M. A. et al. Use of an underlayer for large area crystallization of rubrene thin films. *Chem. Mater.* **29**, 6666–6673 (2017).
32. Park, S.-W. et al. Amorphous-to-crystalline phase transformation of thin film rubrene. *J. Phys. Chem. B* **114**, 5661–5665 (2010).
33. Liu, Y.-X. & Chen, E.-Q. Polymer crystallization of ultrathin films on solid substrates. *Coord. Chem. Rev.* **254**, 1011–1037 (2010).
34. Hasebe, M., Musumeci, D. & Yu, L. Fast surface crystallization of molecular glasses: creation of depletion zones by surface diffusion and crystallization flux. *J. Phys. Chem. B* **119**, 3304–3311 (2015).
35. Tao, J., Mao, G. & Daehne, L. Asymmetrical molecular aggregation in spherulitic dye films. *J. Am. Chem. Soc.* **121**, 3475–3485 (1999).
36. Sun, Y., Zhu, L., Kearns, K. L., Ediger, M. D. & Yu, L. Glasses crystallize rapidly at free surfaces by growing crystals upward. *Proc. Natl Acad. Sci. USA* **108**, 5990–5995 (2011).
37. Mullins, W. W. Flattening of a nearly plane solid surface due to capillarity. *J. Appl. Phys.* **30**, 77–83 (1959).
38. Chai, Y. et al. A direct quantitative measure of surface mobility in a glassy polymer. *Science* **343**, 994–999 (2014).
39. Li, Y., Yao, Z., Wu, L. & Wang, Z. Nonbirefringent bands in thin films of a copolymer melt: rapid rhythmic crystal growth with an unusual crystal–melt interface. *CrystEngComm* **20**, 2221–2226 (2018).
40. Zhu, L. et al. Surface self-diffusion of an organic glass. *Phys. Rev. Lett.* **106**, 256103 (2011).
41. Zhang, Y. et al. Effect of substrate interactions on the glass transition and length-scale of correlated dynamics in ultra-thin molecular glass films. *J. Chem. Phys.* **149**, 184902 (2018).
42. Zhang, W., Brian, C. W. & Yu, L. Fast surface diffusion of amorphous o-terphenyl and its competition with viscous flow in surface evolution. *J. Phys. Chem. B* **119**, 5071–5078 (2015).
43. Paeng, K., Powell, C. T., Yu, L. & Ediger, M. D. Fast crystal growth induces mobility and tension in supercooled o-terphenyl. *J. Phys. Chem. Lett.* **3**, 2562–2567 (2012).
44. Zhang, W., Douglas, J. F. & Starr, F. W. Why we need to look beyond the glass transition temperature to characterize the dynamics of thin supported polymer films. *Proc. Natl Acad. Sci. USA* **115**, 5641–5646 (2018).
45. Yin, S., Shuai, Z. & Wang, Y. A quantitative structure–property relationship study of the glass transition temperature of OLED materials. *J. Chem. Inf. Comput. Sci.* **43**, 970–977 (2003).
46. Agata, Y., Shimizu, H. & Kido, J. Syntheses and properties of novel quarterphenylene-based materials for blue organic light-emitting devices. *Chem. Lett.* **36**, 316–317 (2007).
47. Cheng, J.-A. & Cheng, P.-J. Crystal study of N,N′-diphenyl-N,N′-bis(1-naphthyl)-1,1′-biphenyl-4,4′-diamine. *J. Chem. Crystallogr* **40**, 557–560 (2010).
48. Shin, J.-W. et al. Random nano-structures as light extraction functionals for organic light-emitting diode applications. *Org. Electron.* **15**, 196–202 (2014).
49. Fielitz, T. R., Phenicie, C. M. & Holmes, R. J. Effects of additives on crystallization in thin organic films. *Cryst. Growth Des.* **17**, 4522–4526 (2017).

Acknowledgements

Funding for this work was provided by the NSF Program in Solid-State and Materials Chemistry under grant numbers DMR-1307066 and DMR-1708177. J.S.B. acknowledges support from the NSF Graduate Research Fellowship under grant no. 00039202. The authors acknowledge helpful discussions with C. Teresi, as well as the groups of P. Dauenhauer, C. D. Frisbie and R. L. Penn for the use of their high-speed camera, atomic force microscope and X-ray diffractometer, respectively. Parts of this work were carried out in the Characterization Facility, University of Minnesota, which receives partial support from the NSF through the MRSEC programme.

Author contributions

J.S.B. designed the experiments and analysed the data. T.R.F. made the initial observation and characterization of the pattern formation phenomenon. J.S.B., T.R.F., T.J.S. and J.R.V.S. prepared, annealed and imaged samples. K.S. performed tapping mode AFM measurements. J.S.B. performed peak force AFM measurements. C.P.C. performed XRD measurements. J.S.B., T.R.F. and R.J.H. interpreted the results and wrote the manuscript. All authors discussed and reviewed the manuscript. R.J.H. supervised the work.

Competing interests

The authors declare no competing interests.

Additional information

Supplementary information is available for this paper at https://doi.org/10.1038/s41563-019-0379-3.

Reprints and permissions information is available at www.nature.com/reprints.

Correspondence and requests for materials should be addressed to R.J.H.

Publisher's note: Springer Nature remains neutral with regard to jurisdictional claims in published maps and institutional affiliations.

Methods

TPBi, α-NPD, BCBP and rubrene were purchased from Luminescence Technology Corp. and used as received (sublimed grade). All films were deposited using high-vacuum ($<10^{-6}$ torr) thermal evaporation at a deposition rate of 1 Å s^{-1}. Silicon substrates had a 2-nm-thick native oxide layer and were exposed to a UV–ozone ambient for 10 min before deposition and remained at ambient (25 °C) temperature during deposition. For the surface variation experiments, 10-nm-thick films of Ag (Aldrich Chemistry, 99.999% trace metals basis), Au (Alfa Aesar, 99.9995% trace metals basis) and tungsten (VI) oxide (WO_3, Puratronic, 99.998% trace metals basis) were thermally evaporated on cleaned Si substrates before deposition of TPBi films. Film thicknesses were measured with variable-angle spectroscopic ellipsometry.

Annealing was initiated by placing a substrate onto a homebuilt temperature-controlled microscope stage purged with nitrogen and pre-heated at the annealing temperature. Episcopic optical micrographs were taken with polarized light using a Lumenera Infinity 1.0 camera. The images in Figs. 1d and 3a, Supplementary Figs. 11, 13 and 17c,d were captured with a cross-polarizer to identify grains by birefringence contrast. All other optical micrographs were captured without a cross-polarizer. To improve the visibility of the periodic pattern, histogram equalization was applied to the images in Figs. 1g, 2a,b and 5a and linear contrast stretching was applied to all other images using the scikit-image package in Python (version 3.6).

Atomic force microscopy was conducted using a Bruker Nanoscope V with a Multimode 8. Images in Fig. 2 and Supplementary Fig. 14 were acquired in tapping mode, attractive regime, and AFM cantilevers were aluminium-coated highly doped monolithic silicon with a nominal spring constant of 42 N m^{-1}. Images in Fig. 4 were acquired in PF-QNM mode, and AFM cantilevers were aluminium-coated n-type silicon with a nominal force constant of 0.6 N m^{-1}. Full AFM scan parameters are tabulated in Supplementary Tables 1, 2.

Periodicity in optical microscopy and AFM images was measured using an FFT using the Python package SciPy[50] and Gwyddion[51]. Optical diffraction measurements were performed at normal incidence using a laser with a wavelength of $\lambda = 473$ nm having a spot diameter of 0.8 mm, and images were captured on a 16 cm × 16 cm screen with a camera length of 9 cm (schematic of measurement geometry is shown in Supplementary Fig. 3d). X-ray diffraction patterns were taken in the theta–theta geometry with a Co Kα source ($\lambda = 0.179$ nm).

Crystal growth rates were extracted from in situ optical microscopy time series. Images were histogram equalized, thresholded and despeckled to automate grain boundary detection.

Data availability

The data that support the findings of this study are available from the corresponding author on reasonable request.

Code availability

The code used to analyse pattern periodicity and pattern quality is available at https://github.com/jsbangsund/pattern-image-analysis. The code and interactive graphical user interface used to extract crystal growth rates is provided at https://github.com/jsbangsund/crystal-growth-rate-analysis.

References

50. Jones, J. et al. SciPy: Open source scientific tools for Python. *SciPy* http://www.scipy.org (2001).
51. Nečas, D. & Klapetek, P. Gwyddion: an open-source software for SPM data analysis. *Cent. Eur. J. Phys.* **10**, 181–188 (2012).